5

Electrical and Magnetic Transport of 3d-4f Oxides

The electric, magnetic and dielectric properties of 3d-4f oxides are very interesting and give us possibility to use these oxides in the industrial scale and understanding their unique properties which makes these materials under the scopes of scientific interests. Let us take a look on some examples of these oxides and some results and their analysis.

5.1 Electric Properties of 3d-4f Oxides

The DC resistivity – temperature dependence measurements of $Eu_{0.65}Sr_{0.35}Fe_xMn_{1-x}O_3$ (x=0.1 and 0.5) after sintering at 1350 ℃ for 72 hours are shown in Fig. 5.1. The temperature dependence of the resistivity curve of both samples shows the semiconductor behavior where the resistivity of $Eu_{0.65}Sr_{0.35}Fe_xMn_{1-x}O_3$ decreases with increasing temperature. The relation between resistivity and temperature expressed in the exponential dependence and the well known Arrhenius equation gives the best fitting of the experimental measurements [36];

$$\rho = \rho_0 e^{\frac{-E}{kT}} \tag{5-1}$$

where ρ_0 is the resistivity at room temperature, E is activation energy, k is Boltzmann constant and T is absolute temperature (see fig. 5.1 and fig. 5.2).

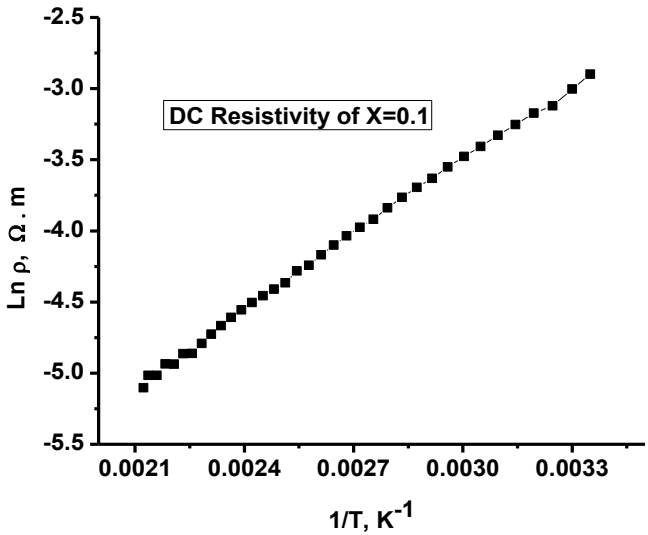

Fig. 5.1 *DC resistivity – temperature dependence of* $Eu_{0.65}Sr_{0.35}Mn_{0.9}Fe_{0.1}O_3$.

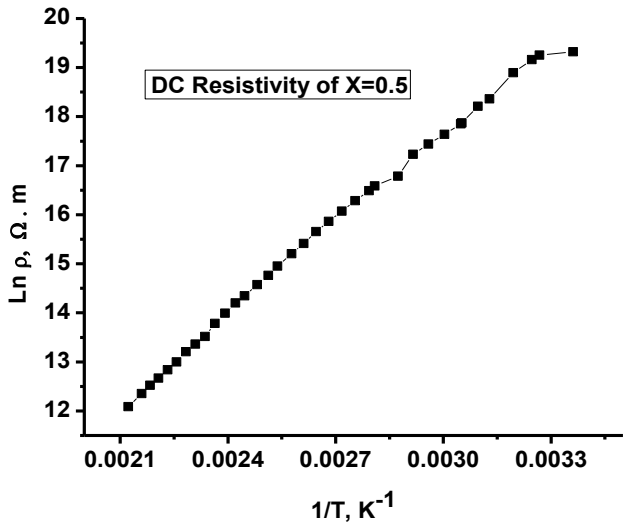

Fig. 5.2 *DC resistivity – temperature dependence of* $Eu_{0.65}Sr_{0.35}\ Fe_{0.5}Mn_{0.5}O_3$.

The electrical conductivity is generally expressed as,

$$\sigma = ne\mu \tag{5-2}$$

where e is the unit charge, n is the concentration of charge carriers and μ is the mobility of charge carriers. The concentration of charge carriers, n is given as

$$n = N.\exp\left(\frac{-E_g}{2KT}\right) = NC \tag{5-3}$$

where E_g is the energy required to create cations of different charges by separating an excited electron from the hole it leaves behind, [73] N is the concentration per formula unit of lattice sites that are available to the charge carriers and C is the fraction of the available lattice sites occupied by the charge carriers.

The mobility of charge carriers, μ is given as

$$\mu = \left[\frac{(1-C)e\ a^2v}{KT}\right]\exp\ (\frac{-E_a}{KT}) \tag{5-4}$$

where a is the lattice spacing, υ is vibration frequency, k is the Boltzmann constant, T is the absolute temperature and E_a is a hopping activation energy [74].

The temperature dependence of conductivity is described in the expressions of n and μ. For oxide semiconductors, n and μ usually increase with temperature. Nevertheless, at equilibrium condition and in air, the concentration of charge carriers is maintained to be constant. Therefore, Eq. (5-3) can be rewritten as $n = NC = Constant$ and thus the temperature dependence of conductivity is described only by μ, as in Eq. (4.4). With Eq. (5-4) being substituted in Eq. (5-2), the expression for the temperature-dependent electrical conductivity of the small polaron material becomes

$$\sigma = \left(\frac{A}{T}\right)\exp\ (\frac{-E_a}{KT}) \tag{5-5}$$

where A is the pre-exponential factor, defined as

$$A = \frac{NC\,(1-C)e^2a^2v}{K} \tag{5-6}$$

The semiconductor-like transport behavior is characterized with three models. (1) a band-gap model (An Arrhenius law), $\rho = \rho_0 \exp\left(\frac{-E_B}{KT}\right)$ is generally used to describe the thermally activated behavior due to a band gap E or a mobility edge; (2) Nearest-neighbor hopping model of small polarons, $\rho = (\rho_0.T)\exp\left(\frac{E_B}{K_BT}\right)$; (3) If the carriers are located in random potential, Mott's a variable - range hopping model (MVRH) expression $\rho = \rho_0 \exp\left(\frac{T_0}{T}\right)^{\frac{1}{4}}$ is appropriate [75]. Thus in order to understand the transport mechanism in $Nd_{0.6}Sr_{0.4}Mn_xCo_{1-x}O_3$, it is necessary to fit the resistivity curves based on these three models.

It has been believed that the electrical properties are controlled by the motion of an e_g electron from Mn^{3+} $(t_{2g}^3 e_g^1 : S = 2)$ to Mn^{4+} $(t_{2g}^3 e_g^0 : S = 3/2)$ via the intervening oxygen.

The influence of annealing on decreasing resistivity for $Nd_{0.6}Sr_{0.4}CoO_3$ composition is shown in ref [76]. One can note high resistivity for as prepared sample while resistivity vanished for sample heated at 850 ℃ which is attributed to the decrease of grain size relatively increases the insulating region due to the enhancement of the grain boundary effects. This behavior is in agreement with the earlier report [77].

The metal behavior for $Nd_{0.6}Sr_{0.4}CoO_3$, which keeps a full metallic-like behavior during temperature range 300–440 K is presented in ref [76]. No sharp peak in ρ is observed at 440 K (T_p) (Metal - insulator transition) but there is accompanied a broad maximum around ~ 440 K T_m, which is attributed to

oxygen deficient components having distribution of oxygen stoichiometry lead to the broad maximum at T_m. [78] These compound has a distinct metallic phase below the transition temperature (T_m) and above this temperature it becomes semiconducting. The (M–S) transition is believed to arise from the increase of Co–O–Co bonding angle. [79]

It is well established that cobalt exhibits different spin state. The low spin (LS, $t_{2g}^6 e_g^0$) state changes to either higher spin (HS, $t_{2g}^4 e_g^2$) or intermediate spin (IS, $t_{2g}^5 e_g^1$) state with increasing temperature [89]. Therefore, the population of Co(IS) changes to LS state at low temperature, which creates an additional distortion in the lattice due to the smaller ionic size of the low spin Co^{3+} ion. A a result, buckling of CoO_6 octahedral increases, which in turn affects the charge transfer integral along the Co-O-Co bonds. This effect is probably the reason for monotonous increase in the resistivity behavior of the Co-containing samples [175] [75].

The linear fitting of ln ($\rho/\ \rho_0$) virius 1/T for x = 0 as prepared sample according to band gap model (thermal activation conduction) (TAC). The activation energy can be calculated using this model to be E_p = 0.529 eV. It can be observed that the semiconductor behavior covered all temperature range for as prepared compound and a little resitivity dependence temperature is observed for heated at 850 ℃ compound, which is attributed to the increase of particles size due to thermal treatments. Fig. 5.3 shows the DC resistivity – temperature dependence of $Nd_{0.6}Sr_{0.4}CoO_3$.

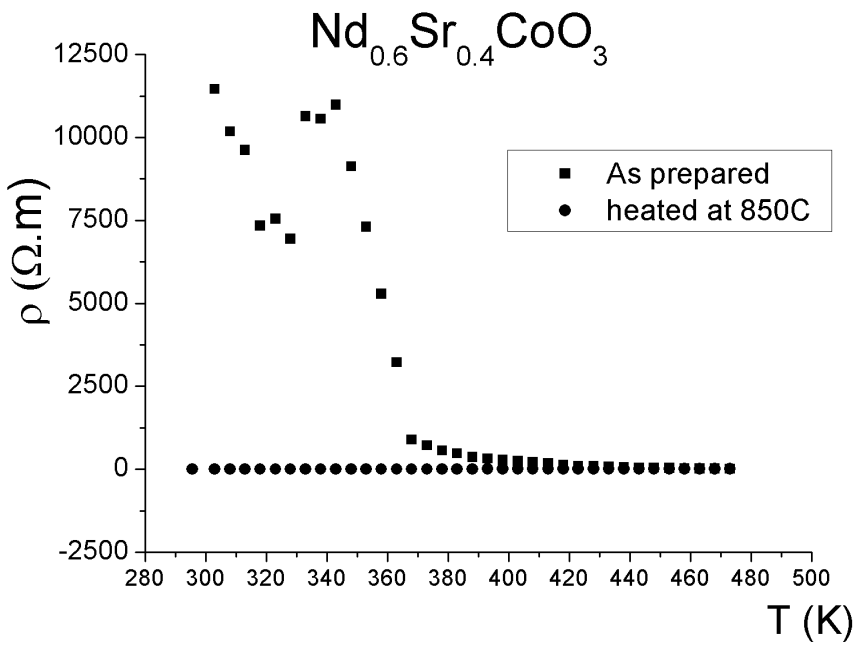

Fig. 5.3 *DC resistivity – temperature dependence of* $Nd_{0.6}Sr_{0.4}CoO_3$.

Similarly, the relation between electrical resitivity and temperature for x = 0.3 as prepared is shown where the semiconductor behavior is noticed in low temperature range, the curve has a peak at T_p = 90 ℃ and beyond T = 90 ℃ the resistivity is suppressed.

For thermal treatment samples the resistivity ρ(T) is so low and temperature independence of the resistivity ρ(T) is noticed. The influence of thermal treatment in decreasing resistivity for $Nd_{0.6}Sr_{0.4}Mn_{0.3}Co_{0.7}O_3$ compound is attributed to the increasing of the particles size. [80]

This large variation in the electrical behaviour could be due to the different annealing treatments which induce an important change in the crystallite and grain sizes, as evidenced by SEM and the comparison of the $D_{h\,k\,l}$ values. It can be considered that the increase of ρ with the reduction of grain size is mainly related

to the increase of both the height and width of tunneling barriers. Evidently, with the grain size decreasing the number of pores and consequently, the porosity increase. The increase of ρ with the grain size decrease is a result of carriers sampling and more grain boundary material. The large volume of grain boundary material produces a greater electrical conductivity change. In these cases, the influence on the electrical transport properties of the mixed valence manganese ions is less important. In fact, it was found that for fine-particle perovskite manganites, an increase in resistivity occurs as the particle size decreases and the grain boundary contribution increases due to the broken Mn–O–Mn bonds at the surface of the smaller articles that impede the conduction. This is a typical behaviour in the case of nanoparticles of the manganite system. [81]

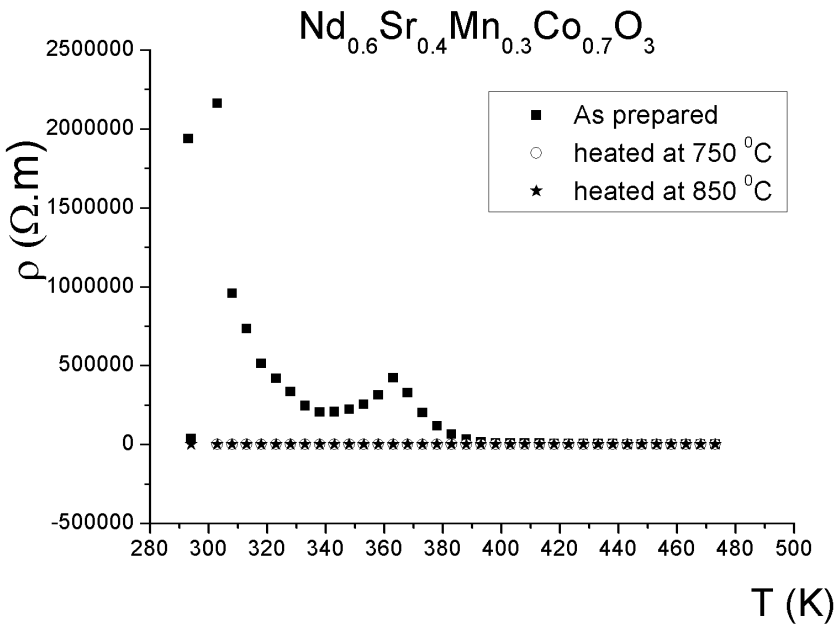

Fig. 5.4 *The DC resistivity – temperature dependence measurements of* $Nd_{0.6}Sr_{0.4}Mn_xCo_{1-x}O_3$ *(x = 0.3).*

The resistivity ρ increases systematically with decreasing grain size over the whole range of temperature. This is not surprising considering that ρ is increasingly influenced by the presence of grain boundaries, which act as regions of enhanced scattering for the conduction electrons and disorder. Isaac et al. and Sanchez et al. showed that the spin becomes heavily disordered at the grain boundary due to the strain with the lowering of the grain size which may result in a growth of the resistivity. It is also seen that the resistivity reduces drastically with grain growth, as the bound- arise of the grains consist of more magnetic disorder than the cores. Gupta et al. explain the variation in properties with grain size as the reflection of magnetic disorder induced canting of Mn spins near the surface of the grains.

From the DC resistivity – temperature dependence of $Nd_{0.6}Sr_{0.4}MnO_3$ composite annealed at 850 ℃ (see Fig. 5.5) it is clear that the semiconductor behavior is well represented with the exponential dependence. According to the well known formula given in equation (5.7) for resistivity – temperature dependence;

$$\rho = \rho_0 \exp\left(\frac{-E}{KT}\right) \tag{5-7}$$

According to this formula one can calculate the activation energy which has the value of E = 0.2154 eV which in good agreement with those reported in ref. [82]

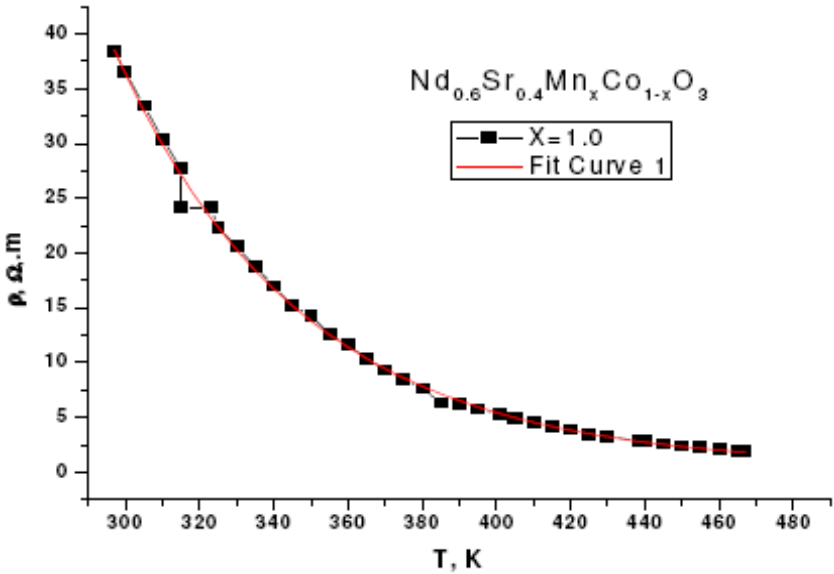

Fig. 5.5 *The DC resistivity – temperature dependence measurements of* $Nd_{0.6}Sr_{0.4}Mn_xCo_{1-x}O_3$ *(x=1).*

The DC resistivity – temperature dependence measurements (Fig. 5.5) of $Nd_{0.6}Sr_{0.4}Mn_xCo_{1-x}O_3$ as prepared showed decrease of resistivity with the increase of temperature which explains the semiconductor behavior of these compounds. From the DC resistivity – temperature dependence measurements it is clear that there are phase transition points at temperatures 338 K, 363.3 K, 358.5 K and 340 K corresponding to x = 0, 0.3, 0.7 and 1, respectively. The semiconductor behavior was noted for all samples without annealing. The observed resistivity for the samples as prepared are too high compared with those annealed. This high resistivity of the sample after chemical reaction without annealing is attributed to the small crystalline size. The crystalline size of the samples without annealing (as prepared) are 15.5 nm, 43.4 nm and 45.6 nm for x = 0, 0.3 and 0.7 respectively.

The DC resistivity – temperature dependence measurements of $Nd_{0.6}Sr_{0.4}Mn_xCo_{1-x}O_3$ after annealing at 850 ℃ for 12 hours are shown in

Fig. 5.4 and Fig. 5.5 (x = 0, 0.3 and 0.7). The temperature dependence of the resistivity curve of the samples where x = 0 shows the metallic behavior and there is transition to semiconductor at T = 443 K. The same behavior is represented by the sample where x = 0.3 but the transition temperature is observed at T = 333 K. In the case of x = 0.7 the behavior is completely different because there is linear relation between the temperature and resistivity indicating the metallic behavior without no transition point. This behavior is ascribed to the presence of an appreciable concentration of Mn^{3+} which introduces a large number of charge carriers (electrons) and facilitates the movement of those charge carriers by hopping mechanism. So the electron hopping between Mn^{3+} and Mn^{4+} can be responsible for both the metallic behavior and the relatively low electrical resistivity exhibited by the substituted phases. [24]

It was found that (ρ) always decreases with increasing temperature for the two compositions. Obviously, the resistivity increases with Co doping. On other hand, the figure shows that the peak transition (M–S) for x = 0.7 at T=313 K. This compound (x = 0.7) has a distinct metallic phase below the transition temperature (T_m) and above this temperature they become semiconducting. The (M–S) transition is believed to arise from the increase of Mn–O–Mn bonding angle [83] for composition with (x = 0.3), there are logarithmic decreasing in resistivity with increasing temperature which is implied the semiconductor behavior. Hence, the composition (x = 0.3) behaves as semiconducting material (no transition).

The reported resistivity results in $LaMn_{1-x}Co_xO_3$ reveal that ρ is increased considerably due to the Co substitution where the value of ρ for x = 0.15 is one order of magnitude lower than that of the value for x = 0. [85] The reported results suggest that Co^{2+} appears as a result of Co substitution which leads to the

charge redistribution, $Mn^{3+} + Co^{3+} \rightarrow Mn^{4+} + Co^{2+}$ Thus, appearance of Co^{2+} causes the increase in ratio of Mn^{4+}/Mn^{3+}, leading to the further enhancement of DE mechanism. [86]

Finally the DE interaction is stronger for Mn^{3+}- O^{2-} - Mn^{4+} in comparison to that of Co^{3+}- O^{2} -Co^{4+}. Then, the ratio of Mn^{3+}/Mn^{4+} decreases with Co content, increasing Co^{3+}/Co^{4+} ratio. The resistivity value increase as the concentration of cobalt ion increases due to suppression of DE that leads to ferromagnetism. [86]

The spin- spin scattering increase as the concentration of Co increases. The activation energy for polaron hopping as well as small polaron stabilization energy is high in the case of Co-substituted system. The number of charge carriers decreases with increasing Co content, as a result of which resistivity values increase [87].

In the present observation, the considerable decrease of ρ due to the small Co substitution might also be involved with the enhancement of DE mechanism which is more dominating than that of the disorder introduced by the Co substitution. The other plausible interpretation for the decrease of ρ is the modification of the grain boundary region due to the Co substitution where Co substitution weakens the grain boundary effect, leading to the considerable decrease of ρ. At low temperature a minimum in the temperature dependence of ρ is observed. The temperature at which minimum is observed, is shifted towards high temperature as a result of minimal substitution.

Fig. 5.7 plots the electrical conductivity (log σT) as a function of temperature versus 1/T, obtained for $Nd_{0.6}Sr_{0.4}Mn_xCo_{1-x}O_3$ (x = 0.3, 0.7) sintered at 750 ℃ temperature. The activation energy of electrical conduction calculated according to Bottger and Bryksin model $\sigma = \left(\frac{A}{T}\right) \exp\left(\frac{-E_h}{KT}\right)$ to be 0.142 and 0.6922 eV for x = 0.3 and x = 0.7 respectively. The activation energy of conduction shows that

these materials are oxide ion conductors. This emphases that the conductivity increases and the activation energy decreases with increasing the manganese concentration as in. [70]

In addition, it is well known that the mechanism of electrical conduction in (R,Sr)MnO_3 (R = Nd, Ce, Ho, Eu, Sm) is by hopping of polarons [12, 16, 24–27, 30]. For conduction to occur, Mn^{3+} and Mn^{4+} should be the nearest neighbours and the electron jumps from Mn^{3+} to Mn^{4+} must be via O^{2-} (i.e. Mn^{3+}–O–Mn^{4+} bonding). As a consequence the activation energy of total conduction can be evaluated using the Arrhenius equation:

$$\sigma = \left(\frac{A}{T}\right) Exp\ \left(\frac{-E_a}{KT}\right) \tag{5-8}$$

where σ is the conductivity, A the pre-exponential factor, k the Boltzmann's constant, T the absolute temperature and Ea the activation energy of conduction. Using Eq. (4.8) the activation energy of conduction values were estimated from the slope of the linear portion of log (σ.T) vs. 1/T.

The activation energies obtained for $Nd_{0.6}Sr_{04}Mn_xCo_{1-x}O_{3-\delta}$ (x = 0.3, 0.7) as substituted samples increases monotonically with Mn content for both sintering temperatures. The more substitution of Mn leads to a higher Mn^{3+} content and, as a consequence, the lowering of the energy barrier for polaron hopping. As mentioned earlier, [87-88] some authors verified that the activation energy values increase with decreasing grain size.

In fact, increasing grain size the interconnectivity between grains increases, which enhances the possibility of conduction electrons to hop to the neighboring sites, thereby decreasing the E_a value. Furthermore, for the Mn-substituted samples the activation energy increases slightly with manganese content, which can be linked to the increase of structural distortions, owing to the enhancement of energy barrier for polaron hopping. [89].

The activation energies for sintering compositions at 850 ℃ according to band gap model $\rho = \rho_0 \exp\left(\frac{-E_p}{KT}\right)$ are 0.141, 0.142, 0.133 and 0.2154 eV for x = 0.0, 0.3, 0.7 and 1.0 respectively. One can note that the increasing in sintering temperature lead to a reduction of the activation energy i.e the activation energy decreases with increasing the manganese concentration as in [105].

The transport mechanisms such as nearest neighbour hopping, Mott's variable range hopping and Efrose - hklovskii's variable range hopping mechanisms can exhibit semiconducting behaviour. In the nearest neighbour hopping process, the donor sites are randomly distributed in space and charge carriers hop to nearest empty donor sites. It is found that the deviation for the nearest neighbour hopping mechanism is the most suitable mechanism for describing the ρ-T characteristics of manganite in the semiconducting region. The obtained activation energies for four compositions are 0.529, 0.541, 0.466 and 0.327 eV for x = 0.0, 0.3, 0.7 and 1.0 respectively. The slight increasing in activation energy E_a with increasing Co content (decreasing Mn content) is attributed to the Co substitution suppresses the DE interaction; hence, the higher activation energy is required for hopping of the e_g electrons. [75]

It is commonly accepted that the electrical conductivity is simultaneously determined by the concentration of charge carriers and their mobility. Table (5.1) shows that the E_a value decline slightly with increasing Mn content. An improved carrier's mobility is confirmed by the decreased E_a value, which implies a decrease in the poloran binding energy or an increase in the bandwidth. [90] As mentioned before, the tolerance factor decreased gradually with increasing Mn doping ratio, which implies a decrease in the bending of (Mn,Co)-O-(Mn,Co) bond and a large degree of bond overlapping. This

variation is beneficial for the Zener double exchange process, and thus contributes to the lowered hopping energy E_a.

However, the slight change in E_a's magnitude is so small as to be neglected influence. Thus it is expected that the enhanced electrical conductivity is primarily attributed to the increased concentration of charge carriers.

Table 5.1 *Activation energy and Mn content and thermal treatment.*

X=0.3		**E_p(eV)**	**x (Mn content)**
E_p(eV)	*Thermal treatment*	0.5290	0.0
0.4840	As prep.	0.4840	0.3
0.1421	750 ℃	0.4660	0.7
0.1420	850 ℃	0.3270	1.0

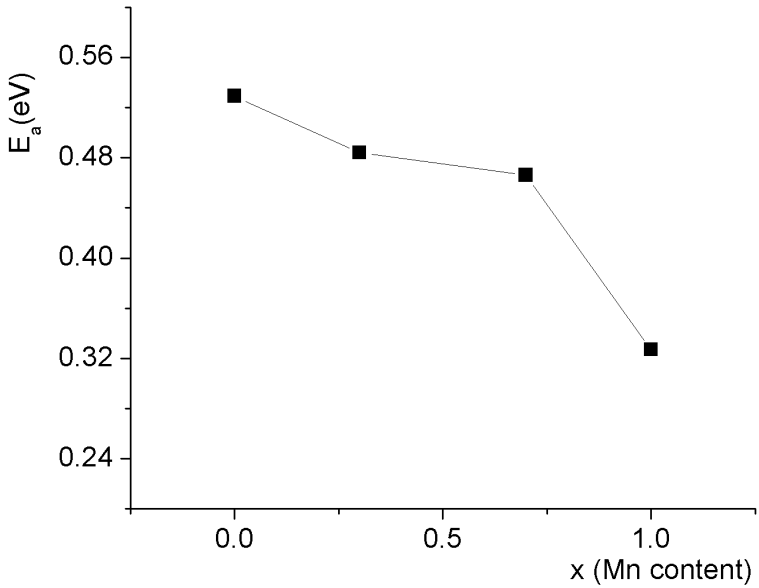

Fig. 5.6 *The relation between concentration of Mn and activiation energy of* $Nd_{0.6}Sr_{0.4}Mn_xCo_{1-x}O_3$.

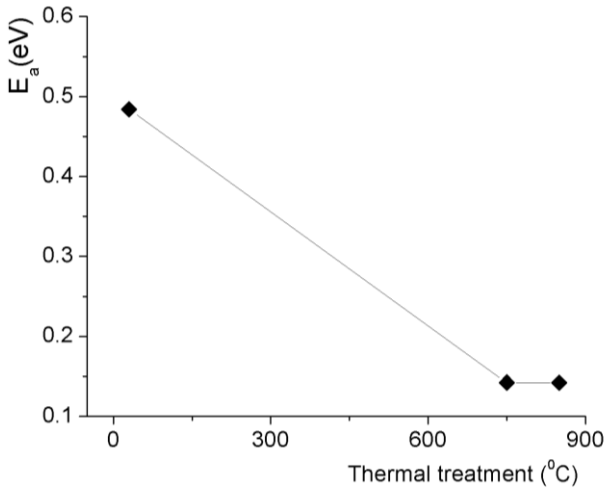

Fig. 5.7 *The effect of thermal treatment on the activation energy of* $Nd_{0.6}Sr_{0.4}Mn_xCo_{1-x}O_3$ *(x = 0.3).*

According to this formula one can calculate the activation energy which has the value of 0.152 eV and 0.535 eV for x=0.1 and x=0.5, respectively. From the linear dependence of the M – O bond length and the volume of unit cell of $Eu_{0.65}Sr_{0.35}Fe_xMn_{1-x}O_3$ on the iron concentration reported by Farag et al [13], one can correlate the increase of increase in the bond length and activation energy of $Eu_{0.65}Sr_{0.35}Fe_xMn_{1-x}O_3$ with the increasing iron concentration. This increase in bond length may explain the increase in the resistivity that is in good agreement with the case of the $Nd_{0.65}Sr_{0.35}Fe_xMn_{1-x}O_3$ in which the increase in the iron content related to the increase in resistivity as reported by Abdel-Latif *et al* [21].

The DC conductivity (σ) can be obtained from the current-voltage (I-V) characteristics at various temperatures $\sigma = \frac{G.t}{S}$, where G being the slope of the linear I-V plot, t is the thickness of the sample and S the sample area. The variations of the conductivity with temperature are usually expressed as

$\sigma = \sigma_0 e^{-E/kT}$. σ_0 can be temperature dependent and another common equation for is; $\sigma = (B/T)e^{-E/kT}$, where B is a constant, E is the activation energy defined as the energy required to release an electron hopping from one ion to the next and k is the Boltzmann constant. The variations of σ with temperature in ferrites is generally attributed to either an increase in the carrier concentration with increasing temperature (band theory) or to a hopping mechanism of electrons between ions of the same element but present in two or more valence states (example Fe^{+2} and Fe^{+3}). In both explanations an increase in temperature should lead to a consequent increase in conductivity.

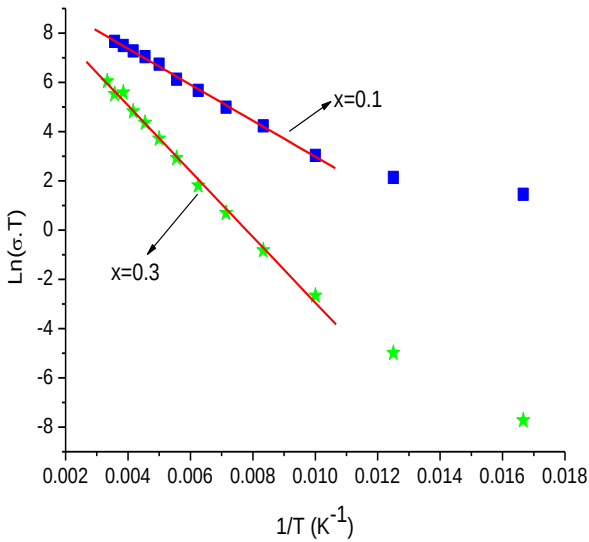

Fig. 5.8 *DC conductivity of $Nd_{0.65}Sr_{0.35}Fe_xMn_{1-x}O_3$ (x=0.1 and 0.3).*

DC conductivity of $Nd_{0.65}Sr_{0.35}Fe_xMn_{1-x}O_3$ (x=0.1 and 0.3) as a function of temperature is illustrated in Fig. 5.8. From the derived conductivities as a function of temperature it turns out that the data is better fitted with the equation $\sigma = (B/T)e^{-E/kT}$.

In fact, the Ln(σ.T) versus 1/T plots for both samples (x=0.1 and x=0.3) shown in figure 5.8 are perfectly linear except at very low temperatures (≤ 80K) where there is a slight deviation and may be a tendency to exhibit a second slope. It is quite clear that in both samples, the conductivity increases with increasing temperature. It is quite remarkable, however, that the increase in σ is by far much more pronounced in the case of the concentration of Iron at x=0.3 than in at the concentration (x =0.1). The activation energies (obtained from the slopes of plots of figure 5.8 are very much different. The obtained activation energy for the sample where x=0.1 is 0.063 eV while it is 0.115 eV for the sample where x=0.3. These activation energies are relatively low which could indicate that over the temperature range considered the samples are in the ferromagnetic regime. It is generally accepted that activation energies are higher in the paramagnetic regime than those in the ferromagnetic case [25]. Furthermore, in some ferrites two slopes are occasionally observed in the Ln(σ.T) versus 1/T plots over two temperature ranges corresponding to two different activation energies [26].

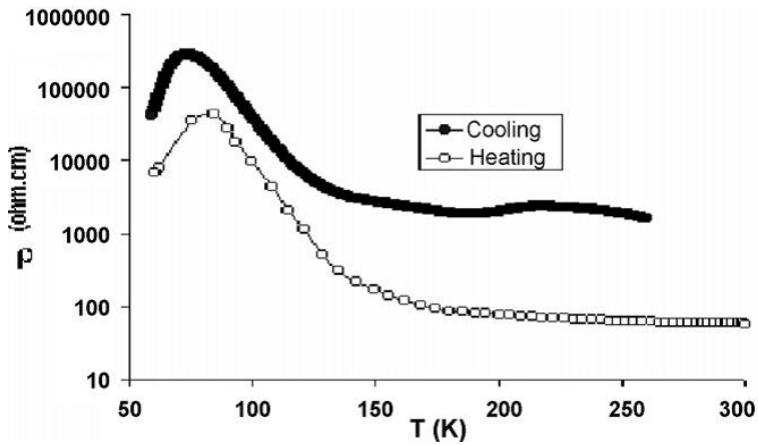

Fig. 5.9 *Temperature variation of resistivity at 0 T magnetic field of $Sm_{0.6}Sr_{0.4}MnO_3$ polycrystalline sample (in heating as well as in cooling).*

The variation in resistivity–temperature dependence behavior of $Sm_{0.6}Sr_{0.4}MnO_3$ at zero magnetic field in the case of heating from the cooling process is shown in Fig. 5.9. The resistivity increases with decreasing temperature, i.e., a semi-conducting behavior is predominant. At temperature of 71 K, a transition is observed on cooling. On heating this transition is shifted a little bit towards higher temperatures. After this temperature (T~74 K) a metallic behavior is observed. This behavior is similar to electron or hole doped manganites [36–40]. A hysteresis between heating and cooling of $\rho(T)$ is characterized. The strontium deficiency leads to an increase in the value of $\rho(T)$ as well as a decrease in the electrical transition temperature. Because we deal with granular materials where there is a possibility to get more or less insulating barriers at the grain boundaries. These barriers will limit the residual resistivity. This mechanism is well known in ceramics, in ferrite as well as in high T_c superconductors where insulating barriers cause the appearance of Josephson junction below the transition temperature of the super-conducting grains. The difference in resistivity is still obtained with applying magnetic field on the sample during the heating and cooling measurements. The dependence of phase temperature on strontium concentration in $Sm_{1-x}Sr_xMnO_3$ was reported in different papers [41-42]. There is a transition, which occurred for $Sm_{0.6}Sr_{0.4}MnO_3$ single crystal at $T_c \approx 107$K (see Ref. [41]) and at $T_c \approx 123$K. which is given in Ref. [42].

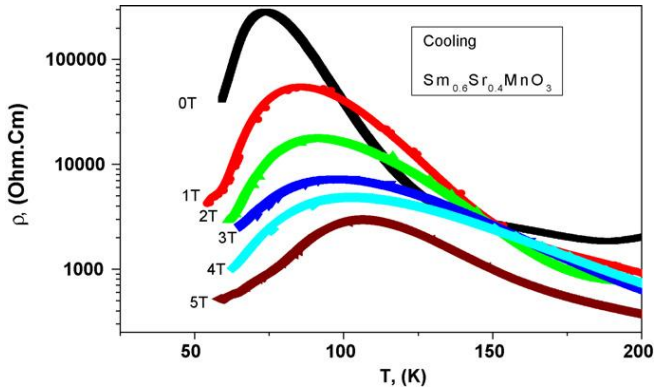

Fig. 5.10 *Thermal dependence of the resistivity at applied magnetic fields of 0 T, 1 T, 2 T, 3 T, 4 T and 5 T of $Sm_{0.6}Sr_{0.4}MnO_3$ for cooling runs.*

For the polycrystalline $Sm_{0.6}Sr_{0.4}MnO_3$ the transition temperature T_c is 125K while T_p is 131K [43]. It was reported by Martin et al. [44] that a transition to charge ordering phase occurred at T_{CO} ~ 140 K. From the above mentioned, in different works, the transition temperature is not the same for $Sm_{0.6}Sr_{0.4}MnO_3$. The crystal structure which is obtained from different works is the same for $Sm_{0.6}Sr_{0.4}MnO_3$. The lattice constants are identical but the oxygen atoms occupy different positions as a result of the tilt of the octahedron. The magnetic and electronic transport occur via oxygen atoms which construct this octahedron. This may lead to the difference in T_c. Also, the coexistence of the ferromagnetic, the canted antiferromagnetic, the charge and the orbital ordering leads to the appearance of the multicritical phase diagram. Looking at the resistivity–temperature dependence in our case (cooling run), one can note the transition from insulator to metallic behavior at T~74 K (see Fig. 5.11). In the metallic state there are two transition temperatures at T~108Kand T~157 K. This may be attributed to the coexistence of charge and canted antiferromagnetic (weak ferromagnetic) ordering at 74 K> T < 108 K. The ferromagnetic ordering predominates at T > 157 K. Similar behavior was reported for $Sm_{0.5}Sr_{0.5}MnO_3$ where the coexisting correlations of the charge or

orbital ordering, ferromagnetic and layered-antiferromagnetic ordering were observed [44].

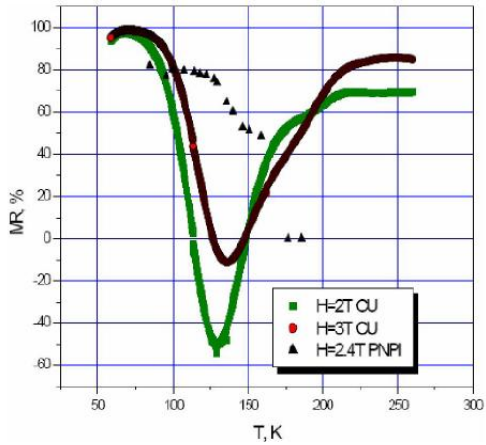

Fig. 5.11 *Magnetoresistance of $Sm_{0.6}Sr_{0.4}MnO_3$ at different applied magnetic fields.*

According to Abdel-Latif and El-Sherbini [4], in spite of both $Sm_{0.6}Sr_{0.4}MnO_3$ samples have the same structure (lattice constant are almost the same) and are prepared using the same method (solid state reaction) they have different MR values [1, 20] as shown in Fig. 5.21. The thermal treatment during preparation, are not the same which may lead to the difference in the tilt of MnO_6 octahedra and hence in the MR values. It is also well known that, the exchange interaction between Mn eg and O2p orbital is governed by the Mn-O1-Mn and Mn-O2-Mn angles which are the basic parameters in determining the magnetic and the electronic behavior of this compound. So we can conclude that the less distortion in the MnO6 octahedra in sample No. 1 (prepared in Cairo University [1]) leads to the increase in CMR value which became more than the corresponding value in sample No 2 (prepared in PNPI [20]).

The DC resistivity – temperature dependence measurements of $YbMnO_3$ is shown in Fig. 5.26. It is clear that as prepared sample has the semiconductor

behavior of this compound as well as the sample which fired at 750°C. Both have the semiconductor behavior but the difference only that as prepared sample has higher resistivity than that one fired at 750°C for 10h. The activation energy of (0.5742eV) of the sample as prepared is higher than the activation energy (0.255eV) of that sample fired at 750°C.

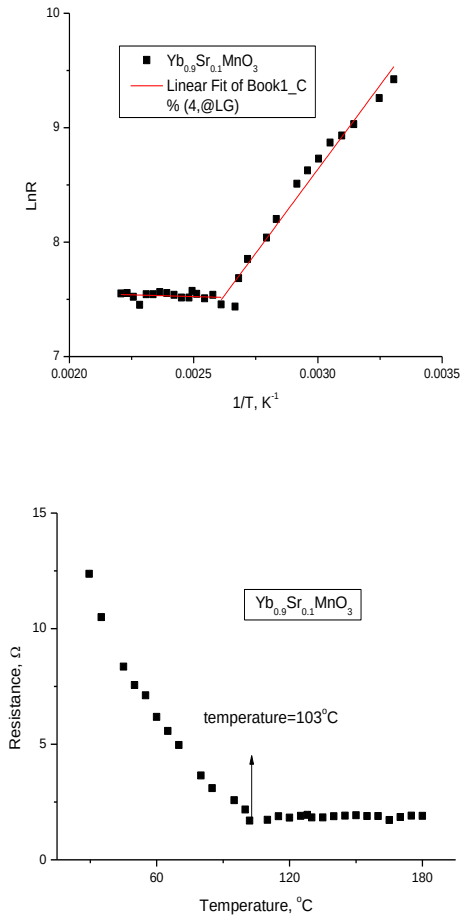

Fig. 5.12 *The DC resistivity – temperature dependence measurements of* $Yb_{0.9}Sr_{0.1}MnO_3$.

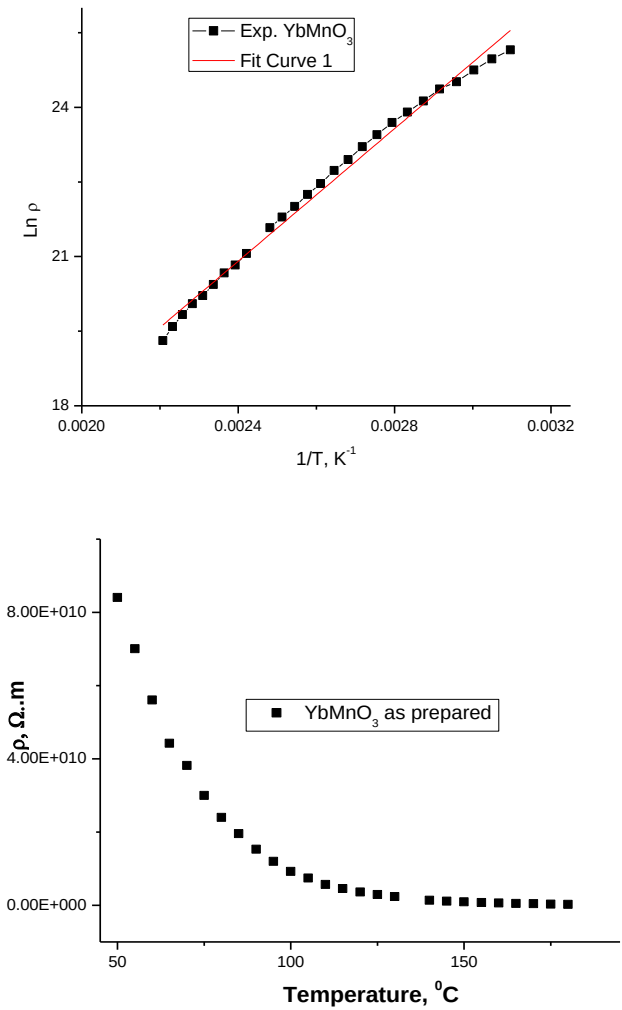

Fig. 5.13 *The DC resistivity – temperature dependence measurements of $YbMnO_3$ as prepared.*

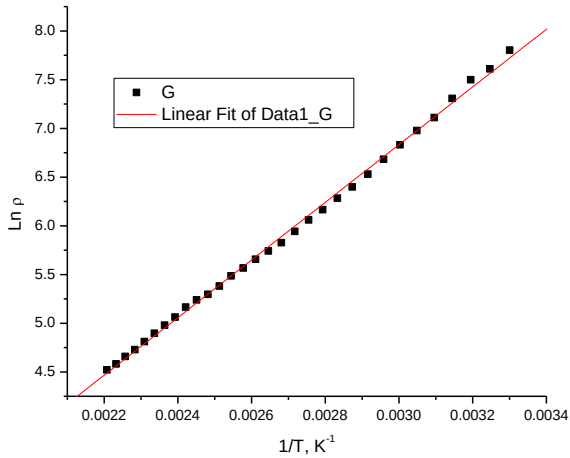

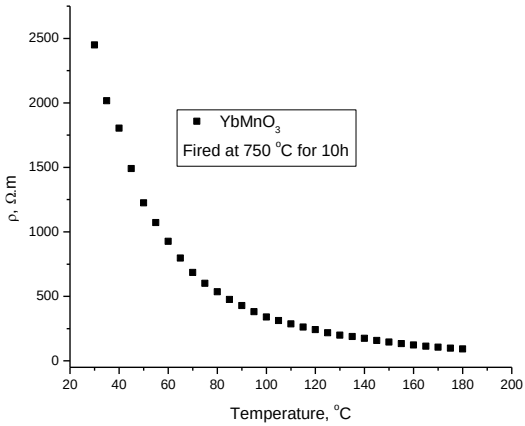

(b) at firing temperature 750 ℃

Fig. 5.14 *The DC resistivity – temperature dependence measurements of* $YbMnO_3$.

5.2 Magnetic Properties of 3d-4f Oxides

The temperature dependence of the magnetization curves of $SmFe_{1-x}Mn_xO_3$ under an applied field H=50 Oe is shown in Fig. 5.15 sad. A paramagnetic-to-weak-ferromagnetic transition with decreasing the temperature is observed for all samples. The corresponding transition temperature, i.e., the Curie temperature sTCd, monotonically decreases as the Mn content increases. It was reported 6 that the parent compound $SmFeO_3$ presents a spin reorientation sSRd at low temperatures Tk=433 Kd from weak-ferromagnetic sWFd ordering to antiferromagnetic sAFd ordering transition as the temperature decreases. The critical temperature sTkd corresponding to this WF–AF transition principally decreases except for the sample with x=0.1d as Fe ions are substituted by Mn ions. For the sample with x=0.3, the transition from WF to AF seems to be almost total with the magnetization less than 0.004 emu/g for T,T_k s=176 K. For the sample with x =0.2, the AF ordering is not totally established and it seems there is a competition between the WF and AF orderings below T_k=350 K since the magnetization is not totally vanished sM, 0.04 emu/g at Tkd. The sample with x=0.1, at first glance, seems to present the same behavior. However, one can observe from Fig. 5.12 sad the initiation of spin reorientation at about T_k=320 K and then WF takes over below 320 K. To explain the changes of these critical temperatures ~T_C and T_k, one has to consider the energies involved corresponding to possible interactions between different M_1–M_2 pairs M_1 and M_2 may be Fe ions or/and Mn ionsd. For the samples with x=0.2 and 0.3, The Mössbauer data show that the samples contain Fe^{3+} ions only, and the possible interactions are Fe^{3+}–Fe^{3+}, Fe^{3+}–Mn^{3+}, and Mn^{3+}–Mn^{3+} pairs. The interaction Fe^{3+}–Fe^{3+} is known to be antiferromagnetic. If we assume that the interaction Mn^{3+}–Mn^{3+} is ferromagnetic as was observed in $La_{1-x}A_xMnO_3$ A=Ca or Sr, the interaction Mn^{3+}–Fe^{3+} seems to be

antiferromagnetic since the AF ordering is well established as the Mn content increases. Moreover, this interaction may be weaker than that of Fe^{3+}–Fe^{3+} which may explain the decrease of *TC* as the Mn content increases. The increases of magnetization for *T*,*Tk* for the sample with *x* =0.1 may be due to the contribution from paramagnetic Sm^{3+} ions. However such contribution should also be expected for the two other samples with *x*=0.2 and 0.3, since the Sm^{3+} ions content was not changed and the interaction between iron smanganesed 3*d* electrons and samarium 4*f* electron ions is much weaker. The substitution of iron by manganese ions may generate different effective internal fields s*Hi*d acting on the central paramagnetic samarium ion leading to different magnetic contribution from Sm^{3+} ions. However the temperature dependence of the magnetizations of the samples with *x*=0.1 and 0.2 in an applied field of 13 kOe are almost identical, as shown in Fig. 5.11 sbd. This suggests that the variations observed in *Ms*T*d at 50 Oe are rather connected to the interactions of *M*1–*M*2 pairs. Unlike the samples with *x*=0.1 and 0.2, the AF magnetic ordering for the sample with *x*=0.3 seems to be not totally broken at 13 kOe. The existence of divalent ions Fe^{2+} - Fe^{2+} being Jahn–Teller ions orbitally frustrated in the sample with *x* =0.1, which yields necessary the presence of Mn^{4+} ions for the charge compensation, may lead to multiple and complex interactions of M_1–M_2 pairs with possibly the existence of ferromagnetic configurations ssuch as the ferromagnetic double-exchange interaction of Mn^{4+}–Mn^{3+} and Fe^{2+}–Fe^{3+}; the interaction Mn^{4+}–Fe^{3+} was demonstrated to be not strong12d that may explain the increase of magnetization at *T*,*Tk* for the sample with *x*=0.1. In addition, the Jahn–Teller effect of Fe^{2+} could be small in the sample with *x* = 0.1 which may reduce the AF coupling and enforce the ferromagnetic coupling. The existence of ferromagnetic ordering is confirmed by the coercivity for the sample with *x* =0.1 of H_c=195 Oe as compared to that of the

samples with x=0.2 and 0.3, with Hc=36 and 32 Oe, respectively. The shape of the hysteresis loop at T=113 K sT,Tkd for x=0.1 shows that the magnetization does not saturate up to an applied field of 13 kOe, with a characteristic slope $[M/]_H$ and slopes were taken in the linear variation of M with H, i.e., above H=5 kOe for all samplesd of 85 memu/g Oe. These features can be correlated to a strong AF interaction dominated by the interaction of Fe^{3+}–Fe^{3+} pairs. For the sample with x=0.2, the slope $[M/]_H$ is of 30 memu/g Oe, indicating that the AF coupling is weaker than that for x=0.1. This result suggests that the substitution of Fe ion by Mn ions weakens the AF coupling $M1$–$M2$ pairs and may be correlated to the weak AF interaction for Fe^{3+}–Mn^{3+}, as suggested above. The hysteresis loop of the sample with x=0.3 shows a similar shape as that for x=0.2 with a slightly greater slope, $[M/]_H$=40 memu/g Oe. However a substantial decrease in the magnetization sat 113 K and maximum field of 13 kOe is observed see Fig. 5.15. This result was expected since the magnetic moment of the free Fe^{3+} ion s5.9mBd is larger than that of Mn^{3+} s4.8mBd.13. The variation in the magnetic properties of $SmFe_{1-x}Mn_xO_3$ upon Mn ion content may also be correlated to the differences in the hybridization of the $t2g$ and O $2p$ electrons.

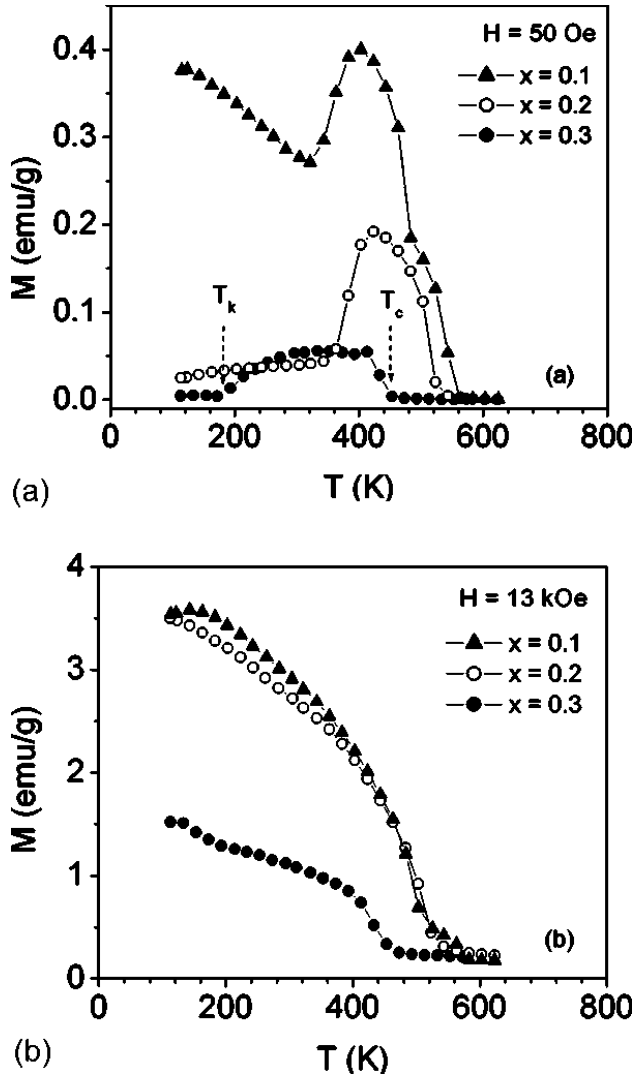

Fig. 5.15 *Temperature dependence of magnetization for the orthoferrites* $SmFe_{1-x}Mn_xO_3$ *(x=0.1, 0.2, and 0.3) in the applied fields of (a) 50 Oe and (b) 13 kOe.*

The resonant inelastic x-ray emission (RIXE) spectra have been measured at the Bach beamline at Elettra synchrotron radiation for the Mn3*d*-2*p*3/2 and also for Fe3*d*-2*p*3/2.

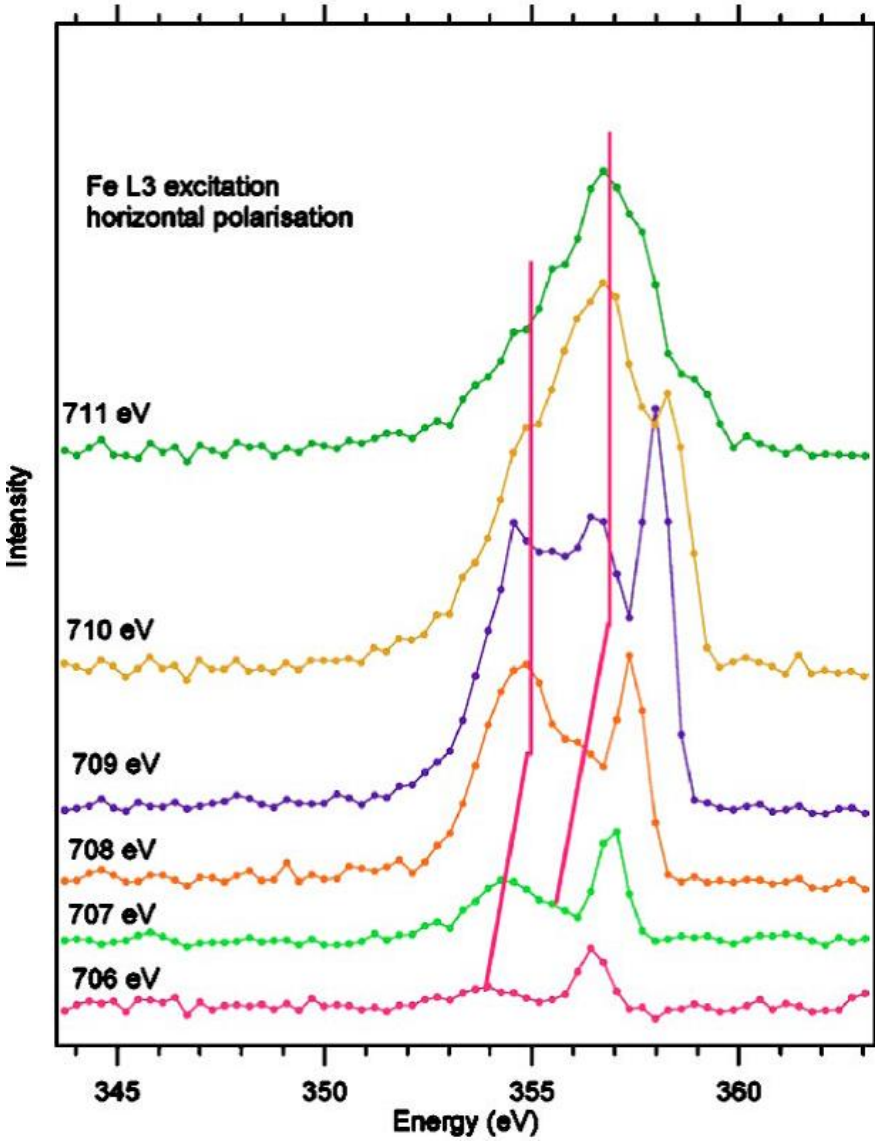

Fig. 5.16 *RIXE spectra of orthoferrite $SmFe_{0.7}Mn_{0.3}O_3$ at room temperature.*

Typical RIXE spectra at Fe *L*3 edges for orthoferrites $SmFe_{1-x}Mn_xO_3$ (x=0.3) are shown in Fig. 5.16. In all spectra, for both Fe and Mn thresholds, resonant and nonresonant features can be easily identified. The nonresonant features

appear at constant emission energy. These structures arise from photon excitation and subsequent x-ray emission and are possibly due to a process in which excitation and emission are incoherent. For instance, the onset of the Mn 2*p*3/2 3*d* excitation is located between 641.5 eV and 642 eV. Resonating inelastic loss features appear at constant energy loss with respect to the elastic peak. Two well-resolved inelastic emission peaks are observed at about 7 eV and at about 2.5 eV below the elastic peak. As for Fe emission, the onset of the Fe 2*p*3/2 excitation threshold is located between 709 and 710 eV. The electronic structure of iron in these compounds seems to be similar to Mn, because the inelastic emission peaks are observed at about 6 eV and at about 2.5 eV below the elastic peak, as is the case for the Mn resonant excitation. As reported in ref [11], Mössbauer data show that the samples contain Fe^{3+} ions only, and the possible interactions are Fe^{3+}–Fe^{3+}, Fe^{3+}–Mn^{3+}, and Mn^{3+}–Mn^{3+} pairs. The interaction Fe^{3+}–Fe^{3+} is known to be antiferromagnetic.

The multi-magnetic states appear either as a result of the inhomogeneity of the iron distributions in the next near neighboring [11, 12] or as a result of the coexistence of ferromagnetic and weak ferromagnetic ordering. The ferromagnetic ordering appears as a result of the Mn^{3+}-O-Mn^{4+} and Fe^{3+}-O-Mn^{3+} interactions, while the antiferromagnetic ordering as a result of Fe^{3+}-OFe^{3+} and Mn^{3+}-O-Mn^{3+} interactions. As a result of the competition between both the ferromagnetic and the antiferromagnetic ordering, the spin glass phase will appear [13-15]. So one can say that the coexistence of the ferromagnetic and weak ferromagnetic ordering is an indication for multi-magnetic states in such compounds while for the sample with x = 0.8 there is only weak ferromagnetic ordering with Curie temperature near 676 K. (See Fig. 5.15)

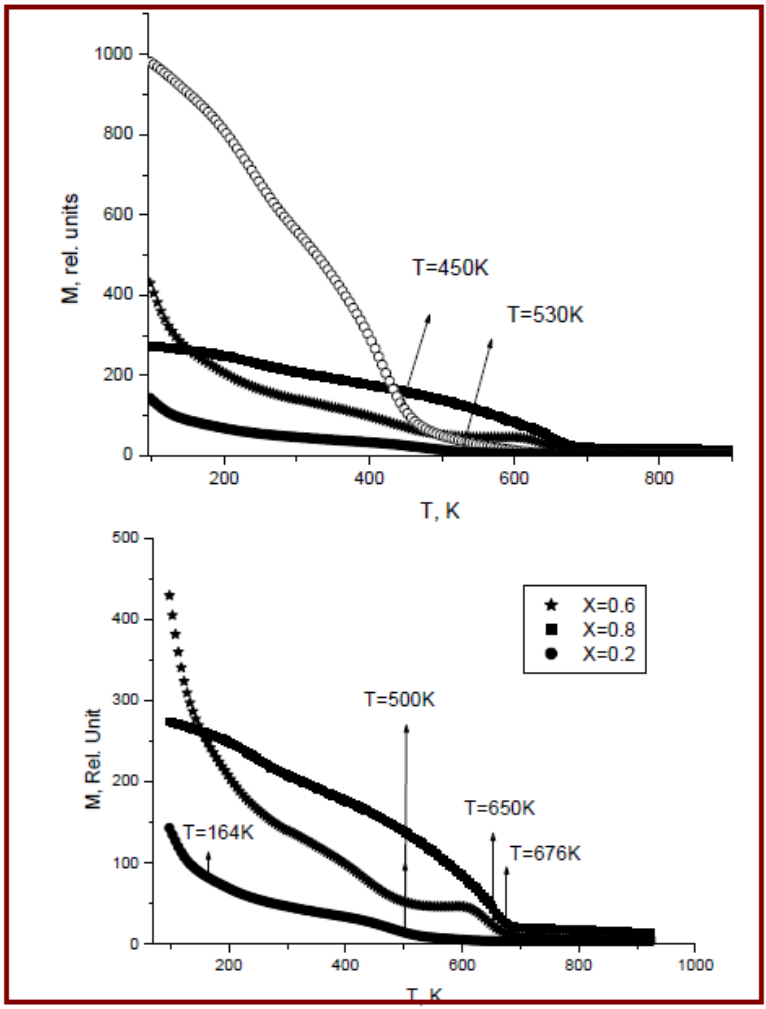

Fig. 5.17 *Magnetic susceptibility of the* $Nd_{0.65}Sr_{0.35}Mn_{1-x}Fe_xO_3$.

In fig. 5.17 we present the variations of the susceptibility with temperature. The figure reveals overall increase in magnetization as the Co contents increase. From the magnetization temperature dependence that is illustrated in Fig. 5.17, it is clear that for x = 0.2, 0.4 and 0.6 there are two phase transition points. These temperatures are indicated by arrows in Fig. 5.17. These results are in a good agreement with those obtained from neutron diffraction for x = 0.6,

where there are two phase transition points; the first transition from ferromagnetic into non-collinear ordering near 500 K and the second from non-collinear into paramagnetic phase near 660 K. According to the Mössbauer spectroscopy measurements at different temperatures for x = 0.4 and 0.6 samples the multi-magnetic states are confirmed [7].

The magnetization temperature dependence behavior of $Nd_{0.65}Sr_{0.35}Mn_{1-x}Fe_xO_3$ in the present case is in a good agreement with those reported for $La_{0.8}Sr_{0.2}Mn_{0.8}Ni_{0.2}O_3$ and $La_{0.7}Sr_{0.3}Mn_{0.8}Ni_{0.2}O_3$ [14], where the antiferromagnetic order is existed in addition to ferromagnetic order and the interaction between them leads to appearance of spin glass [14, 15]. The sample with x=0.0, the magnetization is very weak. The susceptibility shows a low temperature plateau that extends up to 10.5K, above which the susceptibility decreases rapidly to another plateau that extends to 140K. Moreover, the susceptibility shows a wide maximum that is centered around 40K.

As the Co-contents increase, the drop in the susceptibility seen at 140K develops to a sharp peak in x=0.3, and its position shifts to higher Tc (165K). For x=0.7 the peak occurs at 130K and for the Co-free sample, the peak is wide and centered around 175K. The possible magnetic states along with Tc and Co contents are given in Table 5.2.

Table 5.2. *Magnetic phases of* $Nd_{0.65}Sr_{0.35}Mn_{1-x}Fe_xO_3$.

Co-concentration	Tc (K)	Possible Magnetic state
0.0	140	FM (1) below 10K FM (2) between 10-140k
0.3	165	AF below 165
0.7	130	AF below 135
1.0	175	FM below 175

Mössbauer spectra at LN temperature show a superposition of a doublet and magnetic sub-spectra, with increase in the contribution of the latter as Fe

content increases. In the case of x=0.6 the ferromagnetic phase appear in LN temperature which in a good agreement with the neutron diffraction results given in ref. [24]. RT show dominant doublet spectra, but the magnetic sextet is more pronounced on the x=0.6 sample but in this case represent the non-collinear magnetic ordering. The distribution of the hyperfine fields reveals different configurations of Fe^{3+}.

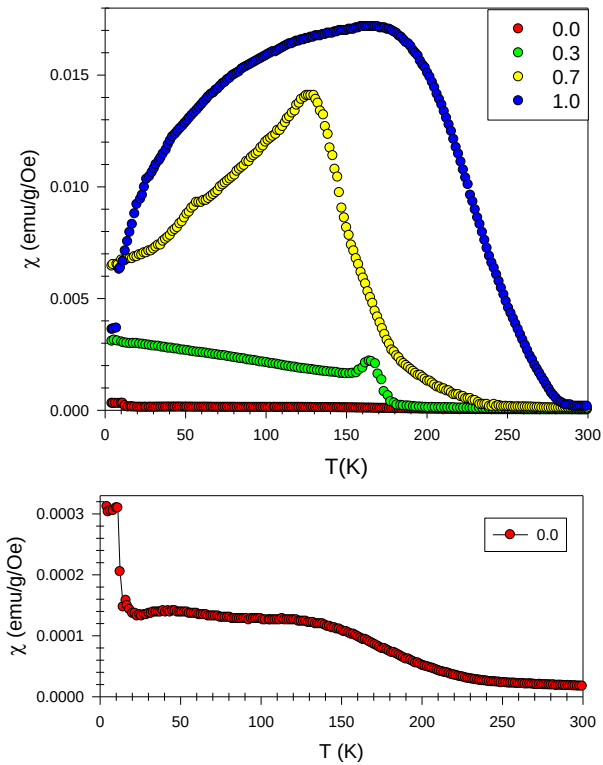

Fig. 5.18 *Magnetic susceptibility of* $Nd_{0.6}Sr_{0.4}\ Mn_xCo_{1-x}O_3$.

From neutron diffraction patterns of $Yb_{0.9}Sr_{0.1}MnO_3$ and $Yb_{0.6}Sr_{0.4}MnO_3$ reported in ref [21] and shown where the antiferromagnetic magnetic ordering is

clear because of the existence of magnetic peaks in these patterns which in good agreement with those works [46] reported before for similar compounds. Integrated intensity of magnetic peak (101) corresponding to antiferromagnetic ordering in hexagonal structure phase of both $Yb_{0.9}Sr_{0.1}MnO_3$ and $Yb_{0.6}Sr_{0.4}MnO_3$ are shown in Fig. 5.19. Mn atoms in the hexagonal structure are located at the center of the MnO_5 bipyramids and are linked by the corner-sharing equatorial oxygens. The displacement of each atom occurs when the temperature decreases below T_N and may lead to a tilt in the MnO_5. [47] From Fig. 5.19, Neil temperature T_N of $Yb_{0.9}Sr_{0.1}MnO_3$ near 87K and T_N of $Yb_{0.6}Sr_{0.4}MnO_3$ near 95K.

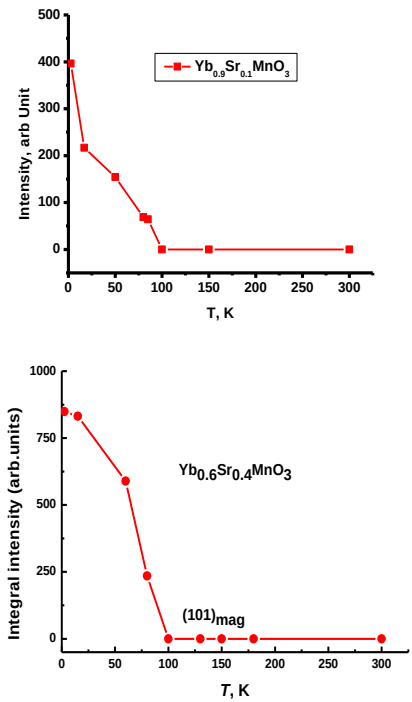

Fig. 5.19 *Integrated intensity of (101) representing antiferromagnetic ordering for $Yb_{0.9}Sr_{0.1}MnO_3$ and $Yb_{0.6}Sr_{0.4}MnO_3$ as a function of temperature.*

According to Capriotti *et al.*, [106-107] the relation between Neil temperature T_N and the nearest neighbor exchange integral J is given by the following formula;

$$T_N \approx 0.3J(S\text{-}1/2)^2$$

where S =2. The deduced values of the nearest neighbor exchange integral J for $Yb_{0.9}Sr_{0.1}MnO_3$ and $Yb_{0.6}Sr_{0.4}MnO_3$ are 11.1meV and 12.1meV, respectively. The DC resistivity – temperature dependence measurements (see Fig. 5.14) of $Yb_{0.9}Sr_{0.1}MnO_3$ showed decrease of resistivity with the increase of temperature which explains the semiconductor behavior of this compound at the temperature range from room temperature up to 103°C. It is noted also that there is transition at temperature t=103°C (or T=476K). From temperature of 103°C and up to 200°C the metallic behavior appeared. The coexistence of hexagonal and orthorhombic crystal systems may lead to the existence of antiferromagnetic and ferromagnetic magnetic ordering on the same for this composite. According to Fabreges et al [27] Néel temperature of $YbMnO_3$ is at T_N~80 K while the ferroelectric transition temperature is as high as T_c~900 K. The antiferromagnetic ordering is the predominant and at the temperature higher than 90K and one can explain the magnetic ordering diagram as follow; at the temperature lower than 90K the ferromagnetic phase will appear and a competition between them lead to a frustration of the net magnetic moment. So the super-paramagnetic semiconductor is the predominant on this temperature range. At the temperature equal to 476 K the metallic behavior is the predominant. The activation energy of first phase (the super-paramagnetic semiconductor) in $Yb_{0.9}Sr_{0.1}MnO_3$ has the value of 0.2527 eV while the activation energy of the second phase (the metallic) is 0.0014 eV.

The Mossbauer spectroscopy measurements were carried out for $SmFe_xMn_{1-x}O_3$ samples at room temperatures [11]. The experimental spectra

are shown in Fig. 5.20. All spectra are fitted using UNIVEM program [5]. The basic M ̈ossbauer parameters are given in Table 5.3. According to the isomer shift δ and quadrupole splitting $\_E_Q$ values, the iron ions in the present compounds are almost trivalent and occupy the octahedral sites [6].

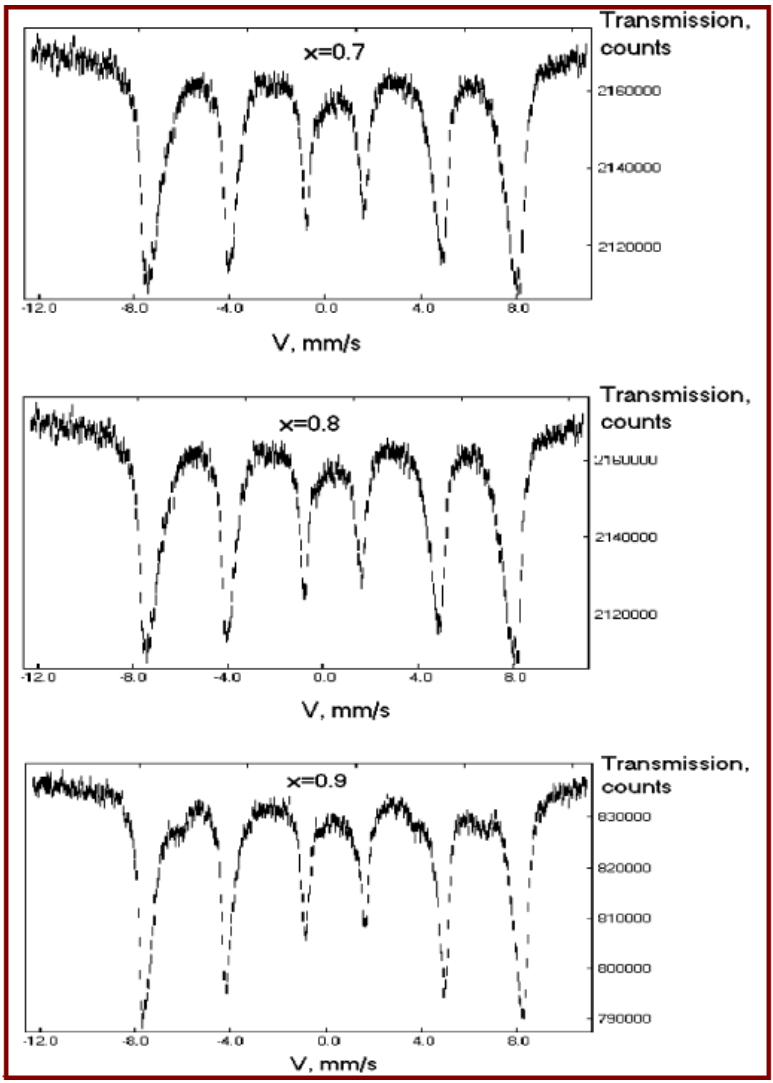

Fig. 5.20 *Mossbauer spectra of* $SmFe_xMn_{1-x}O_3$.

Table 5.3 *Mossbauer Parameters of $SmFe_xMn_{1-x}O_3$.*

Compound	C_i	δ (mm/s)	ΔE_Q (mm/s)	H(KOe)	S_{Exp} %	S_{cal} %
	C_1	0.38	-0.132	459	36	11.8
	C_2	0.37	-0.091	433	34	30.3
$SmFe_{0.7}Mn_{0.3}O_3$	C3	0.37	-0.091	404	22	32.4
	C_4	0.25	-0.029	371	7	18.5
	C_5	0.15	-0.460	294	1	6
	C_1	0.38	-0.121	487	39	26.2
	C_2	0.37	-0.090	465	35	39.3
$SmFe_{0.8}Mn_{0.2}O_3$	C3	0.37	-0.032	437	19	24.6
	C_4	0.25	-0.029	405	5	8.19
	C_5	0.21	-0.460	302	1	1.6
	C_1	0.36	-0.090	498	33	53.1
	C_2	0.36	-0.095	487	11	35.4
$SmFe_{0.9}Mn_{0.1}O_3$	C3	0.35	-0.083	475	31	9.8
	C_4	0.36	-0.080	452	8	1.5
	C_5	0.24	-0.043	405	17	0.1
$SmFeO_3$	C_1	0.54	-0.054	503	100	100

The results of the fitting of the experimental spectrum for $x = 0.7$ sample show that there are five magnetic sextets C_1–C_5. The isomer shift values of C_1–C_4 are close to each other and a good indication for the trivalent iron state while the isomer shift of C_5 are indicative of the divalent iron state [4]. The intensity of the latter sextet 1% is very small and one may neglect it. The quadrupole splitting values of C_1–C_4 show that the iron ions occupy the octahedral site. The hyperfine field Hin the first four sextets decreases systematically within decremental fields of $\_H \approx 29$ kOe (see Table 5.3). In similar way, for the sample with $x = 0.8$, the hyperfine field decreases within $\_H \approx 27$ kOe in the first four sextets and in the case of $x = 0.9$ sample the hyperfine field decreases in steps within $\_H \approx 17$ kOe in the C1–C4 sextets.

The nonrandom cation distribution model, proposed by Bashkirov et al. [7] is used in the present case to interpret the experimental spectra. This model is based

on the contribution of several magnetically split sextets forming the obtained spectra. Each one corresponds to a different iron concentration in the second coordination sphere. According to this model, the monotonic decrease in the hyperfine field is attributed to the decrease in the number of iron ions *n*(Fe) in the octahedral site, where *n*(Fe) takes values from 6 to 0. So from the above results, due to the replacement of iron ions by manganese in the next nearest neighbor (2^{nd} coordination sphere) various sextets were obtained. Every sextet has a hyperfine field that depends on the number of iron cations in the surrounding environments.

The probabilities of the various cation distributions *S*cal calculated using a binomial formula [4] are given in the 7^{th} column of Table 5.3. It is clear that the experimentally obtained probabilities *S* do not agree with *S*cal so that the distribution of iron ions in the octahedral sites is not governed by a random distribution. Such cations are formed together in nonrandom way and these results are in a good agreement with those for $NdFe_xMn_{1-x}O_3$ [8]. On the other hand, in Table 5.3 we included the Mossbauer parameters of $SmFeO_3$ [3]. From these parameters, it is clear that one sextet was obtained because there is only one probability that the Fe ions occupy the octahedral site surrounded by six Fe ions. The difference of hyperfine field (in the case of *n*(Fe) = 6) for $x = 0.9$, 0.8, 0.7 from the value of $x = 1$ may due to the effect of the 3rd coordination sphere that may also contain Mn ions. This value of Mn ions increases with decreasing the concentration of Fe cations.

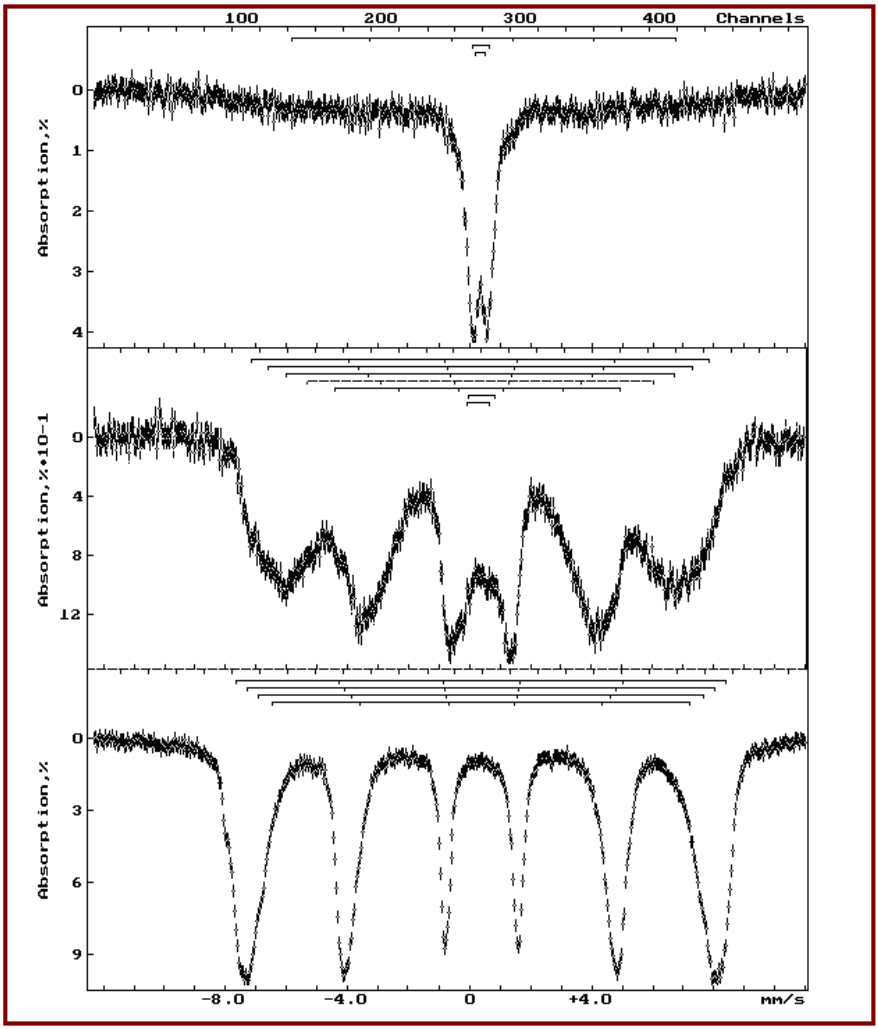

Fig. 5.21 *Mossbauer spectra of NdFex$Mn_{1-x}O_3$ (x=0.4, 0.6 and 0.8).*

Table 5.4 *Mossbauer parameters of $NdFe_xMn_{1-x}O_3$.*

Contents	**C_i**	**δ, мм/с**	**ΔE_Q, мм/с**	**H, кЭ**	**S, %**	**S_{cal}, %**	**n(Fe)**
$NdFe_{0,4}Mn_{0,6}O_3$	C_1	0,34	0,07	390	11	–	–
	C_2	0,36	0,56	–	58	–	–
	C_3	0,34	0,35	–	31	–	–
$NdFe_{0,6}Mn_{0,4}O_3$	C_1	0,37	-0,03	466	12	4,4	6
	C_2	0,36	-0,01	431	14	17,6	5
	C_3	0,36	-0,02	394	20	29,2	4
	C_4	0,37	-0,03	351	18	26,0	3
	C_5	0,32	-0,11	289	21	13,0	2
	C_6	0,39	0,88	–	10	–	–
	C_7	0,31	0,73	–	4	–	–
$NdFe_{0,8}Mn_{0,2}O_3$	C_1	0,38	-0,01	497	31	26,2	6
	C_2	0,38	0,00	475	33	39,3	5
	C_3	0,38	-0,01	451	24	24,6	4
	C_4	0,38	-0,02	423	12	8,1	3

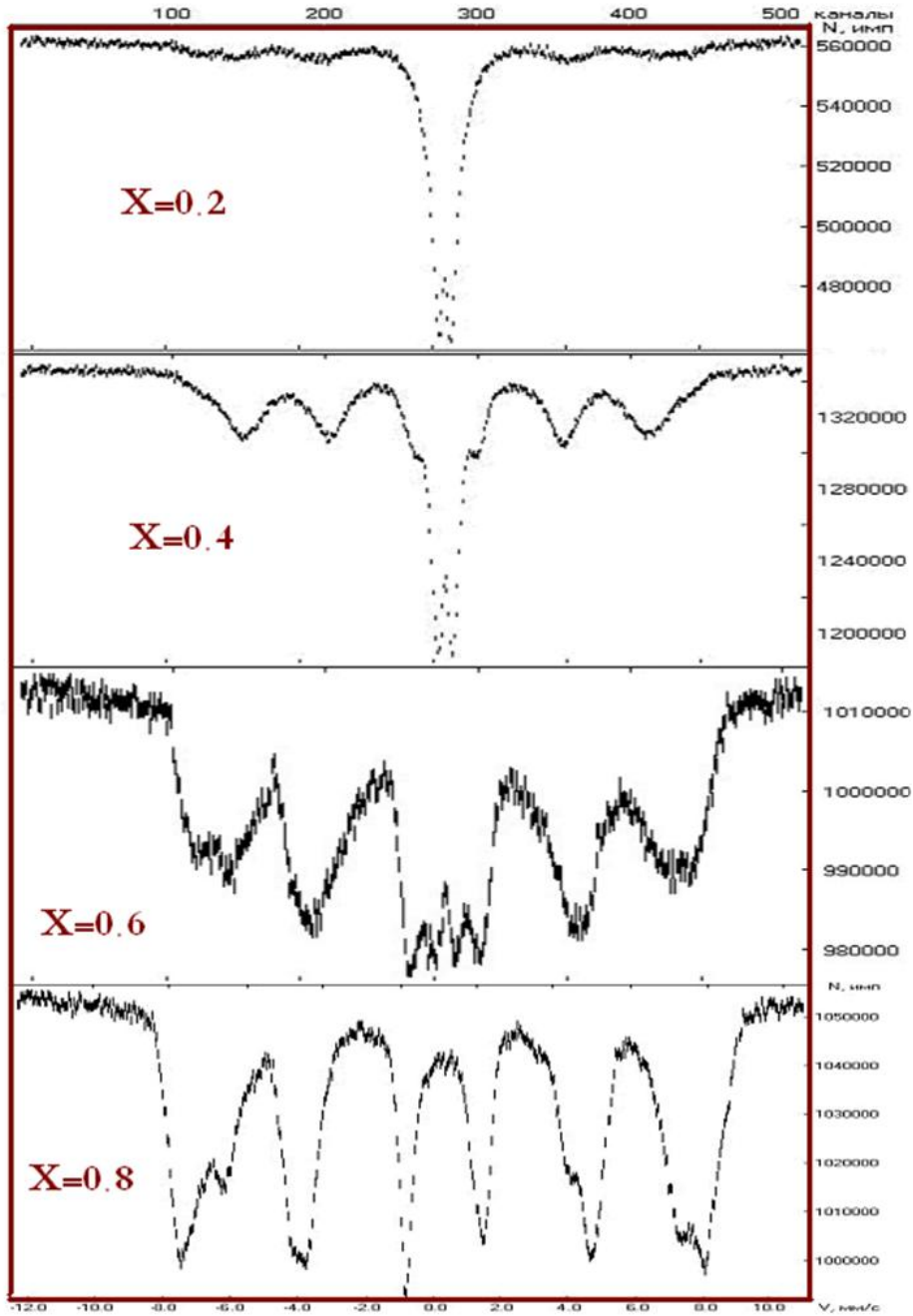

Fig. 5.22 *Mossbauer spectra of* $Nd_{0.65}Sr_{0.35}Fe_xMn_{1-x}O_3$ *(T=287K).*

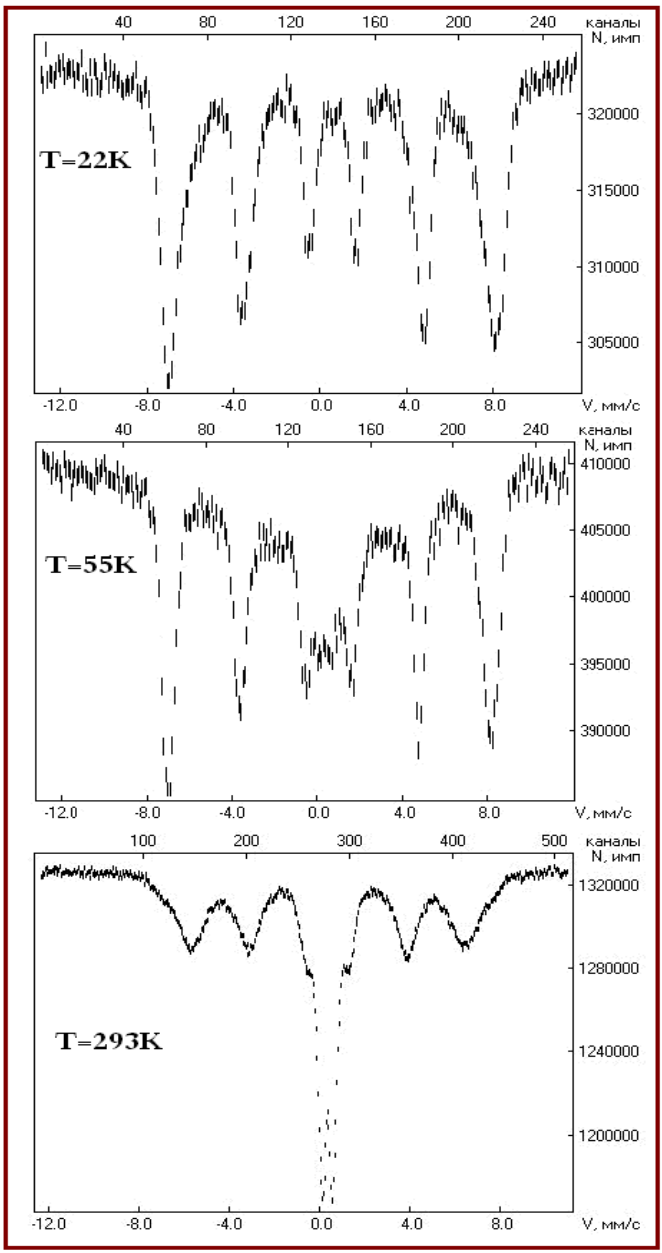

Fig. 5.23 *Mossbauer spectra of* $Nd_{0.65}Sr_{0.35}Fe_{0.4}Mn_{0.6}O_3$ *at different temperatures.*

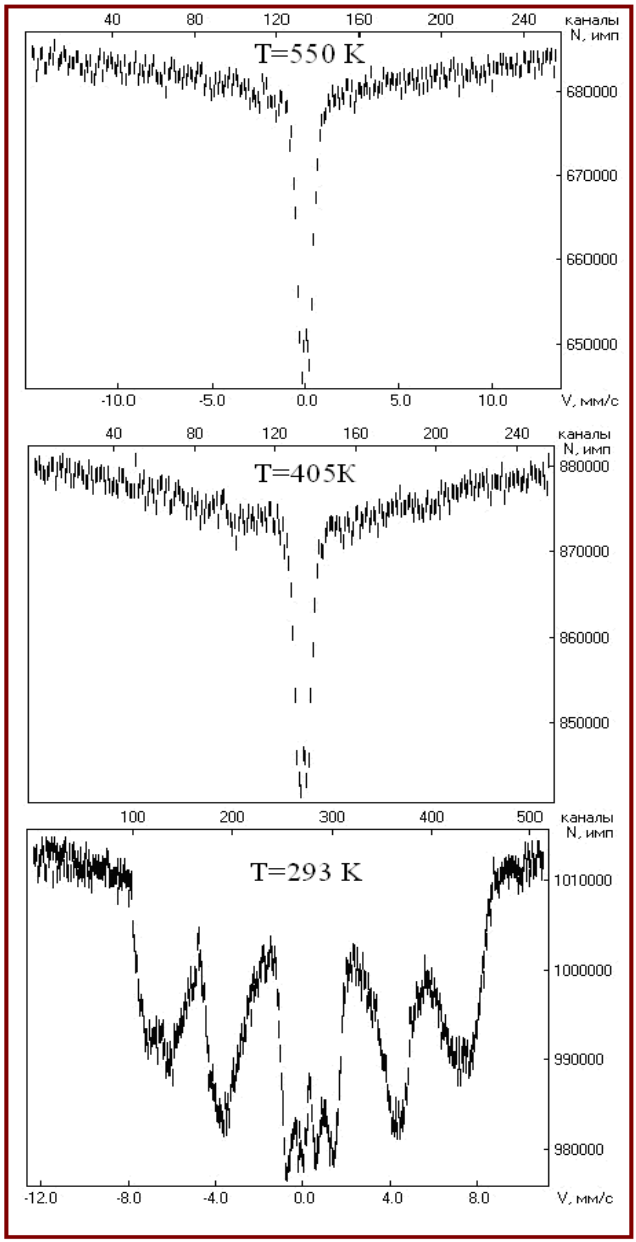

Fig. 5.24 *Mossbauer spectra of* $Nd_{0.65}Sr_{0.35}Fe_{0.6}Mn_{0.4}O_3$ *at different temperatures.*

Mössbauer spectra at LN temperature show a superposition of a doublet and magnetic sub-spectra, with increase in the contribution of the latter as Fe content increases. In the case of x=0.6 the ferromagnetic phase appear in LN temperature which in a good agreement with the neutron diffraction results given in ref. [24]. RT show dominant doublet spectra, but the magnetic sextet is more pronounced on the x=0.6 sample but in this case represent the non-collinear magnetic ordering. The distribution of the hyperfine fields reveals different configurations of Fe^{3+}.

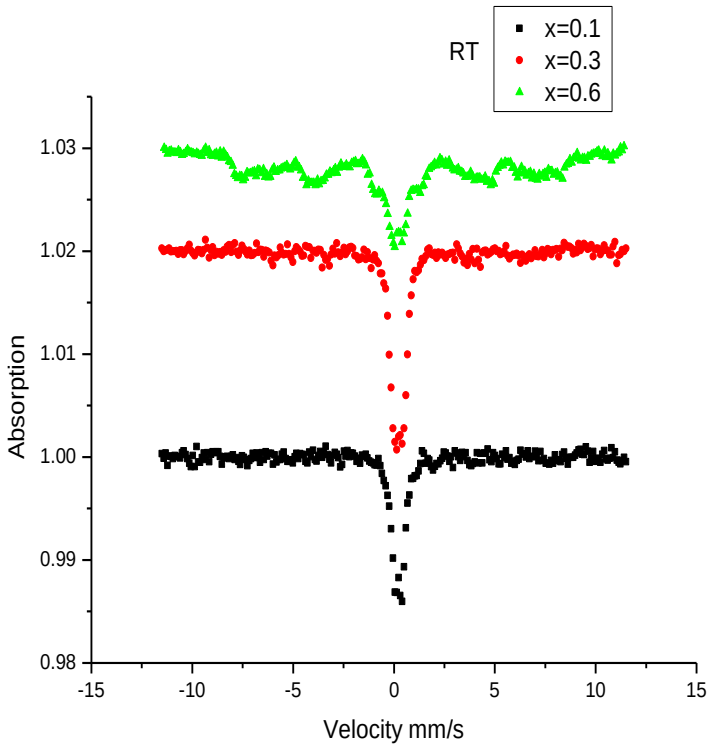

Fig. 5.25 *Mossbauer spectra of* $Nd_{0.65}Sr_{0.35}Fe_xMn_{1-x}O_3$ *at room (RT) temperatures.*

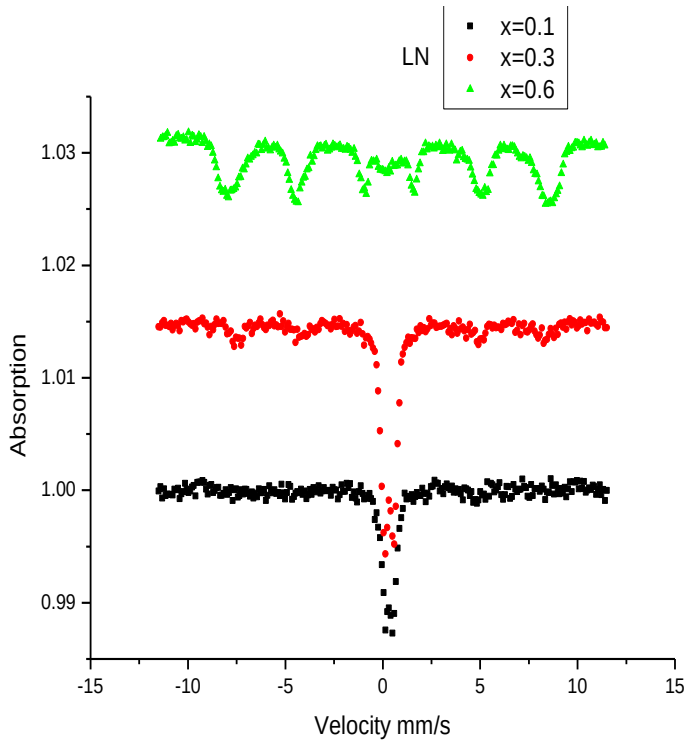

Fig. 5.26 *Mossbauer spectra of $Nd_{0.65}Sr_{0.35}Fe_xMn_{1-x}O_3$ at Liquid nitrogen (LN) temperatures.*

The magnetization measurements at 50 Oe show that the magnetic moment per unit volume as well as the Curie temperature increase with increasing Fe content. The magnetization at 13.5 kOe above T1=220K follow the same trend above. Interestingly, the trend is reversed below that temperature with the x=0.1 sample showing highest magnetization**.**

There is an indication of antiferromagnetic to ferromagnetic spin re-orientation below 200K (T2) in the x=0.1 sample only, but none observed for the x=0.3 or 0.6 samples.

Theoretical model for magnetisation and internal energy of $Eu_{0.65}Sr_{0.35}Fe_xMn_{1-x}O_3$

If we consider the manganese atoms have spin-up and when we dope the manganites with iron, Fe-ions substitute Mn-ions but with spin-down orientation causing antiferromagnetic ordering. With increasing the Fe doping the antiferromagnetic ordering increase and the ferromagnetic ordering decrease. Now we have two states, Mn-sites with a spin-up configuration and Fe-sites with a spin-down configuration.

The simplest theoretical description of that system is called the Ising model. The Ising model which is described earlier in [50] is a simple model of magnetism. The three-dimensional Ising model with two-states consists of N sites ($N = L^3$) where L is the number of sites for each dimension of the lattice. Because we are interested in the simulation of the three-dimensional Ising model for different temperatures and zero magnetic field, the Hamiltonian can be expressed in the form,

$$H = -\frac{J}{2}\sum_{<i,j>}^{N} S_i \,.\, S_j$$

Here, <I,j> refers to a sum over nearest neighbour pairs of atoms and S_i and S_j are the spin in i and i sites. Furthermore, J is called the exchange energy. The 1/2 is to avoid the double counting. The Hamiltonian of the Ising model with applied magnetic field, h, is given as follow;

$$H = -\frac{J}{2}\sum_{<i,j>}^{N} S_i.S_j - h\sum_{1}^{N} S_i$$

When we apply external magnetic field, the ordering of the spins increase, namely, the magnetization increase with increasing the applied external magnetic field.

The symmetry is broken at T_C so that the Monte Carlo simulations give one of the possible ground states and not an average of all of them, This model has been studied using MC simulations on 3d finite lattices with periodic boundary conditions (with size L^3 where L=12). All our simulations have made use of the Metropolis algorithm with averaging performed 10^5 Monte Carlo steps per site. Results were obtained by either cooling down from a high-temperature random configuration as discussed by Banavar *et al.* [51] or heating up from the ground state. The results from the two processes agree with each other.

The internal energy has ground state value equals to 6J/2 because each site has three nearest neighbours, where J is the exchange interaction which is equals to 1 for the antiferromagnetic interaction and to -1 for the ferromagnetic interaction. The internal energy curves continue stable until the transition temperatures, T_C, then, it goes down to an equal value for the whole doping. It is shown that the internal energy for x=0 is the highest value compared with the other x values which have nearly an equal ground state value, 2.7J. At a specific temperature, T=1 J/K, where K is the Boltzmann constant, the internal energy starts at high value at x=0, but it decreases with increasing Fe-doping, x to get its lowest value at x=0.2. The internal energy starts to increase again in the doping range $0.2<x<0.5$.

The ground state of magnetization value decreases with the increase of Fe-doping because the increasing of the spin-down with the increasing of Fe-doping. The magnetization as function of the temperature decreases with increasing of temperature in the range $1.0 > x > 0.5$, while it increase with increase of T for the range $0.5 > x > 0$, this is results because the Fe-content in

$Eu_{0.65}Sr_{0.35}Fe_xMn_{1-x}O_3$ becomes the dominant above x =0.5. We notice that the magnetisation at high-T does not go to zero as usual that is because the compound $Eu_{0.65}Sr_{0.35}Fe_xMn_{1-x}O_3$ always has residual some ordered spins which make the magnetisation has non zero values at high-T.

5.3 Dielectric Properties of 3d-4f Oxides

The dielectric constant ε' (real part) in the investigated system is contributed by several structural and microstructural factors. The real part of the materials was calculated by using the measured capacitance values and dimensions of the pellet by the following formula:

$$\varepsilon' = \frac{Cd}{\varepsilon_o A}$$

where C is the capacitance of the pellet in farad, d the thickness of the pellet in meters,

$$\varepsilon_o = 8.85x10^{-12} Fm^{-1},$$

is permittivity of free space and A is the cross-section area of the cylindrical pellet in m^2. The imaginary part of the dielectric constant ε'' was calculated using the relation: $\varepsilon'' = \acute{\varepsilon} \tan \delta$ where: $\tan \delta = \tan (90 - \phi)$, is the dispersion of the dielectric loss tangent. The plots of dielectric constant $\acute{\varepsilon}$ with frequency at room temperature for the system $Eu_{0.65}Sr_{0.35}Fe_{0.1}Mn_{0.9}O_3$ are shown in Fig. 5.27. A decrease in $\acute{\varepsilon}$ was observed with increase in frequency because at lower frequencies the compound exhibits different types of polarization (i.e. interfacial, dipolar, atomic, ionic and electronic). The observed variation can be explained on the basis of space charge polarization. At higher iron concentration (x = 0.5), the dielectric constant of the sample depends strongly on frequency. The $\acute{\varepsilon}$ decreases with increasing frequency. This shows that space charge polarization contributes more significantly to the

observed dielectric parameters in these compositions. The high value of $\acute{\varepsilon}$ observed in $Eu_{0.65}Sr_{0.35}Fe_xMn_{1-x}O_3$ system shows the ferroelectrics nature of the system. These values at low frequency may be due to voids, dislocations and other defects [43]. High dielectric constant decreases the penetration depth of the electromagnetic waves by increasing the skin effect. The frequency variation of loss tangent (tan δ) of $Eu_{0.65}Sr_{0.35}Fe_xMn_{1-x}O_3$ at room temperature shows that at relatively lower frequencies the values of tan δ is high and decreases rapidly with increasing frequency. The decrease of tan δ with increasing frequency is attributed to the fact that the hopping frequency of the charge carrier can not follow the changes of polarity of the external field beyond a certain frequency [43]. $\acute{\varepsilon}$ and saturated polarizations are dependent on grain size of the materials. However, SEM micrograph shows a granular structure with a dense morphology and little porosity can be seen, which offers much insulating grain boundary, leading to an increase in dielectric constant with decrease in grain size. Broadly speaking, these behaviors may be attributed to the reduced of grain size, compactness and the structural quality of the material.

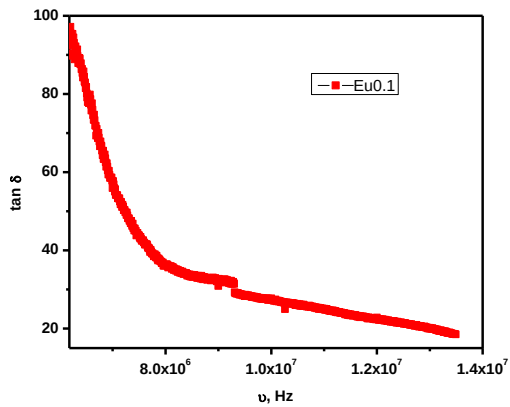

Fig. 5.27 *Dielectric constant ε with frequency at room temperature for the system* $Eu_{0.65}Sr_{0.35}Fe_{0.1}Mn_{0.9}O_3$.

Results show an increase of dielectric constants with increasing the iron content and a decrease with changing the measuring frequency at room temperature. This effect is attributed to the decrease in grain size, compactness and the structural quality of the specimen.

From above results it can be explained that the increase of σ_{ac} with temperature may be attributed to the increase in the drift mobility and hopping frequency of charge carriers with increasing temperature according to relation: $\sigma = ne\mu$, where e is the electronic charge and μ is the mobility of charge carriers and n is the total number of charge carriers per unit volume $n = n_e + n_h$, where e and h refer to the n- and p-type charge carriers, respectively.

The variation of electrical conductivity with frequency at different temperatures for $Nd_{0.6}Sr_{0.4}CoO_3$ as prepared is obviously shown in ref. [76] in which conductivity is increasing slowly at low frequency while increases strongly at high frequency. However, as the frequency increases the conductivity becomes more and more frequency dependent. Sharp drop in conductivity is observed at f = 4.5 MHz which is called the cutoff region. The very basic fact about ac conductivity in disordered solids is that σ_{ac} is an increasing function of frequency. In a hopping model, it is possible to distinguish different characteristic regions of frequencies [11, 12].

At low frequencies where the conductivity is constant, the transport takes place on infinite paths. For a region of frequencies where the conductivity increases strongly with frequency, the transport is dominated by contributions from hopping infinite clusters. Finally, the region where the high frequency cutoff starts to play a role is encountered. The electrical conduction mechanism can be explained in terms of the electron-hopping model. In other words, the conduction mechanism could be due to the electron hopping between two adjacent octahedral sites (B-sites) in the manganite lattice and a transition between $Co^{2+} \leftrightarrow Co^{3+}$ might

take place. Consequently, the increase in frequency enhances the hopping frequency of charge carriers resulting in an increase in the conduction process thereby increasing the conductivity. Further, at high frequencies, the resistivity remains invariant with frequency, because the hopping frequency no more follows the external field and thus lags behind it [13].

The disappearance of the conductivity peak during the decreasing temperature measurements can be attributed to the oxygen exhaustion from the sample during the heating cycle.

This variation in the conductivity may be caused by the oxygen exhaustion from the sample [92] The M-I transition behavior is observed at all frequencies, and the T_p is observed at 370 K at f = 50 Hz, it increases gradually with increasing frequency to reach 420 K at f =5 MHz.

In the case of low-mobility semiconductors such as ferrites, the activation energy is often associated with the mobility of charge carriers rather than their concentration. The charge carriers are considered as localized at the ions or vacant sites and conduction occurs via hopping-type process, which implies a thermally activated electronic mobility. ([100])

The activation energies for all samples at selected frequencies and below 400 K ($T<T_c$) are calculated. The calculated values of the activation energy are listed in Table 5.3. It can be seen that the activation energy decreases with increasing frequency for the studied ferrite which corresponding to ferrimagnetic region. In the ferromagnetic region, the activation energy for electric conduction decreases as the frequency increases corresponding to the thermally activated mobility (hopping conduction model) and not to thermally activated creation of charge carriers, while in the paramagnetic region of disordered state, the increase in frequency has no effect on the conductivity corresponding to thermally activated charge carriers (band conduction

mechanism). [5] The conduction at lower temperatures or below Curie temperature is due to hopping of electron between Fe^{2+} and Fe^{3+}, whereas at higher temperature or above Curie temperature is due to hopping of polarons. [16] Within the ferrimagnetic region of each sample, the activation energies of the prepared samples are found to be in the range 0.32344–0.2415 eV at 100 Hz, The values of E_f in the low frequency region are greater than 0.2 eV in present ceramics and suggests that conduction is due to hopping of charges [191].